

# Design and Simulation of High-performance Planar npp+ Heterojunction CH<sub>3</sub>NH<sub>3</sub>PbI<sub>3</sub> Based Perovskite Solar Cells Using BaSnO<sub>3</sub> ETM and Cu<sub>2</sub>O HTM

Atowar Rahman (✉ [atowar@ru.ac.bd](mailto:atowar@ru.ac.bd))

University of Rajshahi <https://orcid.org/0000-0001-6220-8198>

---

## Research Article

**Keywords:** Organic-inorganic hybrid perovskite solar cells (PSCs), Barium stannate (BaSnO<sub>3</sub>) ETM, Cu<sub>2</sub>O HTM, High power conversion efficiency, SCAPS-1D

**Posted Date:** June 1st, 2021

**DOI:** <https://doi.org/10.21203/rs.3.rs-441744/v1>

**License:**  This work is licensed under a Creative Commons Attribution 4.0 International License.

[Read Full License](#)

---

# Design and simulation of high-performance planar $\text{npp}^+$ heterojunction $\text{CH}_3\text{NH}_3\text{PbI}_3$ based perovskite solar cells using $\text{BaSnO}_3$ ETM and $\text{Cu}_2\text{O}$ HTM

M. Atowar Rahman

Received: date / Accepted: date

**Abstract** In recent years, organic-inorganic hybrid perovskite solar cells (PSCs) have received more and more attention due to their high photovoltaic (PV) performance, potentially high efficiency, simple cost-effective, scalable, and vacuum-free fabrication techniques. However, the performance of PSCs is unstable when exposed to continuous illumination, humidity, and high temperature, which hinders the development of commercialization in the long run. The use of inorganic materials as photogenerated carrier transport layers can enhance the stability of PSC. In this report, we designed a PSC model with a novel  $\text{npp}^+$  heterojunction cell structure of  $\text{Al}/\text{ITO}/\text{BaSnO}_3/\text{CH}_3\text{NH}_3\text{PbI}_3/\text{Cu}_2\text{O}/(\text{Cu or Mo})$  and analyzed the structure by varying the thickness and carrier concentration of each constituent layer, working temperature, and back-contact metal work function using SCAPS-1D solar cell simulator. The simulation addresses, in particular, the role of the  $\text{BaSnO}_3$  as electron transport materials (ETM) and  $\text{Cu}_2\text{O}$  as hole transport materials (HTM) for the device performance. Using  $\text{BaSnO}_3$  and  $\text{Cu}_2\text{O}$  as ETM and HTM, respectively, this article presents the optimization of cell parameters to improve device performance with a predicted power conversion efficiency (PCE) of 32% for the modeled PSC. The proposed novel structure for PSC showed very good PV performance stability on elevated temperature with the temperature coefficient of PCE of only  $-0.112\% \text{K}^{-1}$ .

**Keywords** Organic-inorganic hybrid perovskite solar cells (PSCs) · Barium stannate ( $\text{BaSnO}_3$ ) ETM ·  $\text{Cu}_2\text{O}$  HTM · High power conversion efficiency · SCAPS-1D

---

M. Atowar Rahman  
Department of Electrical and Electronic Engineering, University of Rajshahi, Rajshahi-6205, Bangladesh.  
Tel.: +880-721-711309  
Fax: +880-721-750064  
E-mail: atowar@ru.ac.bd

## 1 Introduction

Solar energy is the fastest growing renewable energy in the world, and the net solar power generation is growing at a rate of about 8.3% every year [1]. At present, 98% of the global market share is consists of seven commercial photovoltaic (PV) technologies, of which thin-films PV technology, with a current growth rate higher than that of crystalline silicon technology, only accounts for 13% of the total [2]. Thin-film PV technologies can reduce manufacturing costs, improve conversion efficiency, and has excellent stability to harness solar energy under different environmental conditions, thereby providing more possibilities for integrating solar cell modules with buildings [3]. Only a few commercial thin-film technologies, such as CdTe and Cu(In,Ga)(S,Se)<sub>2</sub> (CIGS), have achieved PCE of more than 20% [4]. Despite remarkable advances such as considerable PCE, low-cost and fast manufacturing technology, smallest carbon footprint and lowest water use of CdTe technology, the use of toxic and rare earth materials Cd is a limiting factor for the industrial scalability of CdTe technology [5]. PCE higher than CdTe solar cells and use of non-toxic elements are the great success of CIGS technology. So far, the highest PCE of CIGS solar cells reached in Lab is 23.35% [4]. However, the manufacturing technology of CIGS solar cells has proven to be more complicated than Si and CdTe technology, as it contained four different elements, thereby controlling film composition is a big challenge to commercialization of CIGS solar cells. Moreover, CIGS solar cells are expensive as compared with more economical Si or CdTe solar cells, as it consists of scarce elements like gallium (Ga) and indium (In) [6–9]. Solar cells based on the p-type kesterite based semiconductors with copper, zinc, tin, and sulfur/or selenium (CZTS or CZTSe) as components stand out from other thin-film solar energy harnessing materials for being composed of low-cost, earth-abundant, and nontoxic elements. It was first identified as a suitable absorbing material in 1988 [10] and according to literature, the record efficiency of CZTS/CZTSe based TFSCs has increased from 0.66% in 1997 [11] to 12.6% in 2013 [12,13]. However, 31% theoretical PCE of CZTS-based solar cells have been achieved by forming favourable band alignment between the buffers and the absorber layer and reducing non-radiative recombination at the interfaces [14, 15]. The relatively low practical PCE of kesterite-based solar cells is attributed to the larger potential fluctuations and high defects density in the absorber layer, which in turn reduces the open-circuit voltage ( $V_{oc}$ ) drastically.

In recent years, hybrid halide perovskites (CH<sub>3</sub>NH<sub>3</sub>PbI<sub>3</sub>) have attracted extensive research interest as promising light harvesting materials (LHM) and turn out to be one of the most important proprietary technologies in the photovoltaic society because of their suitable optoelectrical properties, high efficiency, and low fabrication costs. Initially, PSCs showed PCE of 3.81% using methylammonium lead halide (MAPbI<sub>3</sub>) perovskites in 2009. In 2011, G. Park et al. synthesized MAPbI<sub>3</sub> quantum dots using iodine-based redox electrolyte and showed PCE of 6.5% [16]. However, the problem of device instability due to the dissolution of perovskite in the polar liquid electrolyte and concerns about the lead content of halide perovskites still exists [16]. Using solid-state hole transport materials (HTM), J. Burschka et al. improved the stability of PSCs and demonstrated a stable PCE of 13% in 2013 [17]. After achieving breakthrough PCE in 2013, a variety of synthesizing technologies have been used in order to achieve a PCE of 20.1% [18–23]. The current record PCE for PSCs is 25.5% in 2020 [24], which is comparable to

silicon-based cell and attracts more attention. According to the detailed balance principle [25], it is predicted that the perovskite-based heterojunction solar cell should achieve a maximum PCE of 37%. With the improvement of stability [26, 27], the effect of defects is reduced to an acceptable level [28, 29], and the energy band offset between LHM and ETM or HTM is still the main factor for hindering PCE of PSCs [30–34].

PSCs with a conventional planar structure consists of an absorber layer made of perovskite materials, deposit between an HTM and an ETM. There are various inorganic and organic materials in hand to scheme the PSC. The overall performances of all the devices depend on the careful choice of these components. Two factors should be carefully considered while selecting materials for electron and hole transport layers: first, the material’s ability to extract and transport charges, and second, the alignment of energy levels in the different layers. In almost all architectures used for PSCs, it is essential to use HTM to extract holes from the perovskite and transport them to the back-electrode. To date, the most employed HTM for PSCs is Spiro-OMeTAD, reported by U. Bach et al. more than two decades ago [35]. However, it was found that the charge mobility was not optimum in Spiro-OMeTAD and its semiconducting properties can be improved by using cobalt-based dopants and ionic salt [36]. Moreover, the high cost and low stability of HTMs like spiro-OMeTAD and PTAA make them unsuitable for commercialization of high-performance PSCs. In addition, PSCs based on organic HTM suffer from degradation in moisture and air. The stability issues of organic HTMs are mostly attributed to the additional dopants and additives, so development of dopant-free organic HTM is another pathway to achieve a high stability and the PCE over 23% based on the dopant-free organic HTM has been delivered [37]. On the other hand, an HTM-free perovskite solar cell is an alternative option to achieve air and moisture stability [38].

Inorganic materials have been investigated as HTMs due to their inherently high stability, high hole mobility, and low fabrication cost. Inorganic HTM for PSCs such as CuI, CuO, NiO, and copper thiocyanate (CuSCN) have received a lot of attention [39, 40]. The PCE of PSCs using aforesaid inorganic HTMs was an encouraging value, but not competitive. Therefore, it is necessary to find highly stable and suitable HTM and ETM for PSCs to show air-stable PCE for a long time. In DSSC and in OPV devices, p-type nickel oxide (NiO) has been successfully used as a HTM due to its wide band gap. In this context, Cu<sub>2</sub>O is used as the HTM for PSCs in this study, due to its ideal band gap, improved charge mobility, and stability over Spiro-OMeTAD and other organic HTMs. M. I. Hossain reported that the device including Cu<sub>2</sub>O as hole transport material among the aforementioned HTMs showed the highest PV performance [41].

ETMs such as SnO<sub>2</sub>, TiO<sub>2</sub>, ZnO, PCBM, C-60, etc. have been researched due to its ability to increase the cell performance significantly by collecting electrons more efficiently and reducing electron-hole recombination at the absorber/ETM interface [42, 43]. The most common metal-oxide ETM for high-performance PSCs are mesoporous and planar TiO<sub>2</sub>. However, due to the low carrier transport and mobility properties of TiO<sub>2</sub>, it suffers from strong recombination of electrons [44]. As the ETM layer in PSCs, nanorods, zinc oxide (ZnO) and nanoparticles lead to PCE as high as 15.9% and 11.1%, respectively [45, 46]. Baena et al. reported a highly efficient planar PSC with a PCE of 18 % using SnO<sub>2</sub> as an ETM [47]. Uniform deposition of PCBM as ETM on the perovskite layer and maintain high

electron mobility are critical issues. Chen et al. adopted NiO and doped NiO as ETM and achieving PCE of 16.2% with device stability was more than 7 days [48]. In this study, we propose to use inorganic barium stannate ( $\text{BaSnO}_3$ ) (perovskite crystal structure) as the ETM of PSC for the first time. The main motivation for using  $\text{BaSnO}_3$  as ETM is due to its suitable conduction band offset (CBO) (+0.03 eV) at the  $\text{BaSnO}_3/\text{CH}_3\text{NH}_3\text{PbI}_3$  interface, very low optical absorption in visible range, high electron mobility at room temperature [49], and its ability to block holes because of its deep valence band (VB) position. Moreover, because  $\text{BaSnO}_3$  has the same crystal structure as  $\text{CH}_3\text{NH}_3\text{PbI}_3$ , the dislocation and defect density of the  $\text{BaSnO}_3/\text{CH}_3\text{NH}_3\text{PbI}_3$  interface will remain low, thereby improving the interface quality. In addition, the large bandgap of  $\text{BaSnO}_3$  can reduce light absorption in the same layer. In this work, we introduce and numerically assess the novel npp<sup>+</sup> heterojunction PSC with the following device configuration (Al/ITO/ $\text{BaSnO}_3$ /  $\text{CH}_3\text{NH}_3\text{PbI}_3$ /Cu<sub>2</sub>O/Cu or Mo) by SCAPS-1D. Here, Cu (111) with the metal work function of 4.94 eV [50] or Mo is used as back contact materials, while, Al is used as front contact materials. The PV performance parameters are studied by tuning the back-contact metal work function, working temperatures and the thickness, carrier concentration, defect density of different layers to obtain an optimum cell performance.

## 2 Numerical modelling and simulation parameters

Simulation can show the physical operation, the feasibility of the proposed physical model, and is a basic method to understand the operation of the device, and how the device parameters immediately affect the physical operation and performance of the solar cell device without spending a lot of money and waiting for a long time. Planar heterojunction structure was adopted for  $\text{CH}_3\text{NH}_3\text{PbI}_3$  based perovskite solar cells with the layer configuration of front contact (Al)/ITO/ $\text{BaSnO}_3$ / $\text{CH}_3\text{NH}_3\text{PbI}_3$ /Cu<sub>2</sub>O/back contact (Cu or Mo). In this work, we use the Solar Cell Capacitance Simulator (SCAPS-1D) to analyse the photovoltaic (PV) performance of  $\text{CH}_3\text{NH}_3\text{PbI}_3$  based perovskite solar cells. SCAPS-1D is based on the solution of three governing transport equations in semiconductor; Poisson's equation, continuity equations for free electrons and holes [51]. Under one-dimensional and steady-state conditions, SCAPS is capable of solving these three coupled differential equations and then calculates the electrostatic potential and the quasi-Fermi level for holes and electrons at all point in the solar cell and finally calculate the carrier concentrations, electric fields, and other device performance parameters. The material parameters of various layers, as it is important and ultimately determine the relative accuracy of simulated results, are selected precisely from authentic literature. In some cases, input parameters are taken from reasonable assumptions to reflect the possible results under actual experimental conditions. Table 1 lists the essential parameters for different layers of the device and their values used to perform the simulation. A single-level defect with Gaussian energetic distribution is introduced into the bulk region of each semiconductor layer. Losses due to recombination at each interface ( $\text{CH}_3\text{NH}_3\text{PbI}_3/\text{BaSnO}_3$  and  $\text{Cu}_2\text{O}/\text{CH}_3\text{NH}_3\text{PbI}_3$ ) is accounted by introducing reasonable neutral interfacial defects, shown in Table 1. The work function, reflectivity, and surface recombination velocity are the characteristic features of the front and back contact materials. The reflectivity at

Table 1: Material parameters used for simulating (Al/ITO/BaSnO<sub>3</sub>/CH<sub>3</sub>NH<sub>3</sub>PbI<sub>3</sub>/Cu<sub>2</sub>O/Cu or Mo) solar cell [41, 58–60].

Parameters	ITO	BaSnO <sub>3</sub>	CH <sub>3</sub> NH <sub>3</sub> PbI <sub>3</sub>	Cu <sub>2</sub> O
Layer type	Window	ETM	Absorber	HTM
Conductivity type	n	n	p	p <sup>+</sup>
Thickness (nm)	50	50–150	400 – 1150	150
Bandgap E <sub>g</sub> (eV)	3.5	3.16	1.55	2.17
Electron affinity, χ (eV)	4.5	3.90	3.93	3.21
Relative permittivity ε <sub>r</sub>	8.9	17	6.5	7.11
Effective conduction band density of states N <sub>C</sub> (cm <sup>-3</sup> )	2.2×10 <sup>18</sup>	1.2×10 <sup>19</sup>	2.2×10 <sup>18</sup>	2.02×10 <sup>17</sup>
Effective valance band density of states N <sub>V</sub> (cm <sup>-3</sup> )	1.8×10 <sup>19</sup>	1.8×10 <sup>19</sup>	1.0×10 <sup>18</sup>	1.1×10 <sup>19</sup>
Electron thermal velocity (cms <sup>-1</sup> )	10 <sup>7</sup>	10 <sup>7</sup>	10 <sup>7</sup>	10 <sup>7</sup>
Hole thermal velocity (cms <sup>-1</sup> )	10 <sup>7</sup>	10 <sup>7</sup>	10 <sup>7</sup>	10 <sup>7</sup>
Electron mobility, μ <sub>n</sub> (cm <sup>2</sup> V <sup>-1</sup> s <sup>-1</sup> )	10	200	10	200
Hole mobility, μ <sub>p</sub> (cm <sup>2</sup> V <sup>-1</sup> s <sup>-1</sup> )	10	25	10	80
Donor concentration, N <sub>D</sub> (cm <sup>-3</sup> )	10 <sup>21</sup>	10 <sup>17</sup> –10 <sup>22</sup>	0.0	0.0
Acceptor concentration, N <sub>A</sub> (cm <sup>-3</sup> )	0.0	0.0	10 <sup>14</sup> –10 <sup>18</sup>	10 <sup>17</sup> –10 <sup>22</sup>
Defect type	Acceptor	Acceptor	Donor	Donor
Energetic distribution	Gaussian	Gaussian	Gaussian	Gaussian
Peak defect density, N <sub>t</sub> (eV <sup>-1</sup> cm <sup>-3</sup> )	10 <sup>16</sup>	10 <sup>16</sup>	10 <sup>14</sup> –10 <sup>17</sup>	10 <sup>16</sup>
Characteristic energy (eV)	0.1	0.1	0.2	0.1
Reference energy (eV)	0.6	0.6	0.6	0.6
Electron capture cross section for acceptor defect (cm <sup>-2</sup> )	10 <sup>-15</sup>	10 <sup>-15</sup>	–	–
Hole capture cross section for acceptor defect (cm <sup>-2</sup> )	10 <sup>-15</sup>	10 <sup>-15</sup>	–	–
Electron capture cross section for donor defect (cm <sup>-2</sup> )	–	–	10 <sup>-15</sup>	10 <sup>-15</sup>
Hole capture cross section for donor defect (cm <sup>-2</sup> )	–	–	10 <sup>-15</sup>	10 <sup>-15</sup>
Defect density at Cu <sub>2</sub> O/CH <sub>3</sub> NH <sub>3</sub> PbI <sub>3</sub> interface (cm <sup>-2</sup> )			1.0×10 <sup>16</sup>	
Defect density at BaSnO <sub>3</sub> /CH <sub>3</sub> NH <sub>3</sub> PbI <sub>3</sub> interface (cm <sup>-2</sup> )			1.0×10 <sup>16</sup>	

Table 2: Front and back contact parameters used in simulation.

Parameters	Back contact electrical properties	Front contact electrical properties
Surface recombination velocity of electrons (cms <sup>-1</sup> )	1.0×10 <sup>5</sup>	1.0×10 <sup>7</sup>
Surface recombination velocity of holes (cms <sup>-1</sup> )	1.0×10 <sup>7</sup>	1.0×10 <sup>5</sup>
Work function (eV)	4.94 Cu (111) or 4.95 (Mo)	4.26 (Al)
Working temp. (K)	290 – 400	

the front and back contact is assumed to be 10 % and 90 % respectively [52], while other parameters for the front contact, back contact, and working temperatures are shown in Table 2. In this simulation, experimental optical absorption coefficient of the Cu<sub>2</sub>O, CH<sub>3</sub>NH<sub>3</sub>PbI<sub>3</sub>, BaSnO<sub>3</sub>, and ITO thin films are taken from the literature [53–56]. The device was illuminated with a standard AM 1.5G solar spectrum with the power of 100 mW/cm<sup>2</sup> from the window layer (ITO) side [57]. In the simulation process, assuming that the value of the series resistance (R<sub>s</sub>) and the shunt resistance (R<sub>sh</sub>) is ideal, and the operating temperature of the device is 300 K.

### 3 Results and Discussions

#### 3.1 Device structure and energy band diagram

Planar heterojunction structure has been adopted for  $\text{CH}_3\text{-NH}_3\text{PbI}_3$  based solar cells with the novel layer configuration of (Al/ITO/BaSnO<sub>3</sub>/CH<sub>3</sub>NH<sub>3</sub>PbI<sub>3</sub>/Cu<sub>2</sub>O/Cu or Mo), shown in Fig. 1(a). The planar configuration is considered an evolution of the device structure. The simplicity of the planar device structure of PSCs has attracted researchers in the field of thin-film PV cells. In this structure, aluminum (Al) and copper (Cu)/molybdenum (Mo) are used as front and back contact materials, while BaSnO<sub>3</sub>, CH<sub>3</sub>NH<sub>3</sub>PbI<sub>3</sub>, and Cu<sub>2</sub>O are used as ETM, LHM and HTM, respectively, forming the main part of the device. Highly transparent ITO is used as a window layer of the device. As we mentioned earlier that energy level alignment is an important factor affecting cell performance. Both the short circuit current and the open-circuit voltage are affected by the energy level mismatch at the two interfaces. Photo-generated electrons are injected from the perovskite to ETM, while holes from perovskite to HTM. To effectively extract photoelectrons at the ETM/perovskite interface, the conduction band minimum of ETM should be slightly higher in potential than that of the perovskite, while the extraction of holes at the HTM/perovskite interface requires that valence band maximum (VBM) energy of HTM should closely match with the valence band of the perovskite [61]. The simulated energy band diagram of the device using Cu<sub>2</sub>O as HTM and BaSnO<sub>3</sub> as ETM is displayed in Fig. 1(b).

It can be seen from Fig. 1(b) that a small “spike” CBO is formed at the BaSnO<sub>3</sub>/CH<sub>3</sub>NH<sub>3</sub>PbI<sub>3</sub> interface. Therefore, photogenerated electrons in the absorption layer can easily transport through the BaSnO<sub>3</sub> ETM layer into the collection electrode (front contact). At the same time, photogenerated holes cannot enter and recombine with electrons at the BaSnO<sub>3</sub>/CH<sub>3</sub>NH<sub>3</sub>PbI<sub>3</sub> interface, as the valence band energy of BaSnO<sub>3</sub> ETM layer is much lower in potential than CH<sub>3</sub>NH<sub>3</sub>PbI<sub>3</sub> absorber layer. It is also worth noting that the conduction band energy of Cu<sub>2</sub>O HTM layer is reasonably higher than that of the CH<sub>3</sub>NH<sub>3</sub>PbI<sub>3</sub> absorber layer, so that photogenerated electrons from the absorber layer cannot enter into the Cu<sub>2</sub>O HTM layer, thereby reducing recombination losses at the CH<sub>3</sub>NH<sub>3</sub>PbI<sub>3</sub>/Cu<sub>2</sub>O interface. The VBO between the Cu<sub>2</sub>O HTM and CH<sub>3</sub>NH<sub>3</sub>PbI<sub>3</sub> absorption layer is very small, which can ensure an easy and efficient transport of photogenerated holes from CH<sub>3</sub>NH<sub>3</sub>PbI<sub>3</sub> absorber layer to the back electrode through the Cu<sub>2</sub>O HTM layer. Therefore, Cu<sub>2</sub>O and BaSnO<sub>3</sub> form suitable junctions at both sides of the CH<sub>3</sub>NH<sub>3</sub>PbI<sub>3</sub> absorption layer to facilitate the transportation of photo-generated carriers to the respective electrodes and reduce the recombination loss at interfaces. Fig. 2 depicts the J-V characteristics and external quantum efficiency (EQE) spectra of CH<sub>3</sub>NH<sub>3</sub>PbI<sub>3</sub>-based solar cells with (Al/ITO/BaSnO<sub>3</sub>/CH<sub>3</sub>NH<sub>3</sub>PbI<sub>3</sub>/Cu<sub>2</sub>O/Cu or Mo) device structure. The proposed cell exhibited an open circuit voltage ( $V_{oc}$ ) of 1.306 V, short circuit current density ( $J_{sc}$ ) of 27.296 mA/cm<sup>2</sup>, fill factor (FF) of 89.87% and power conversion efficiency (PCE) of 32.04%.

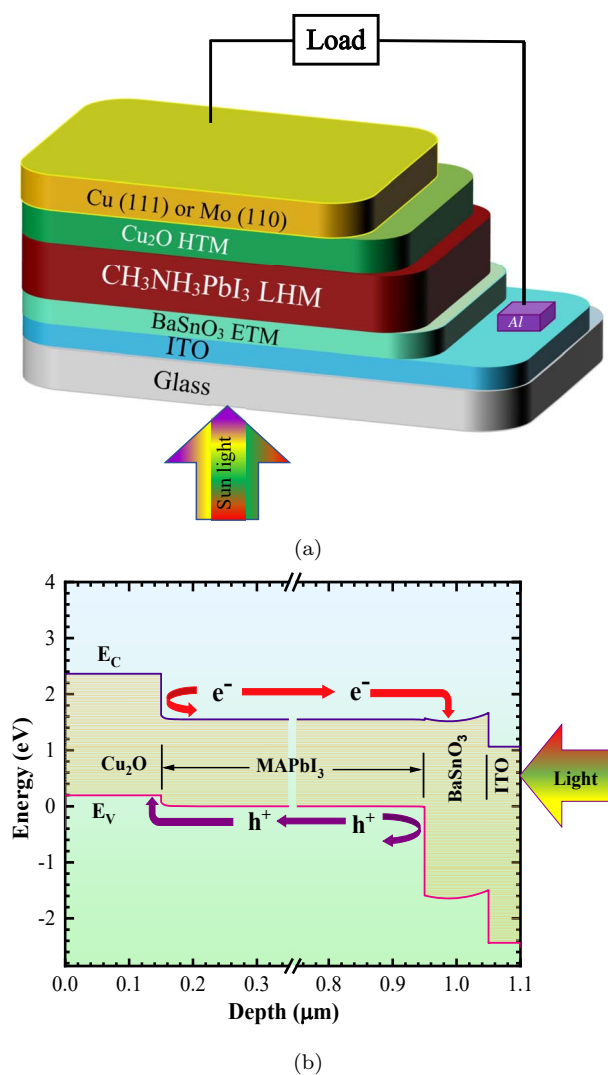


Fig. 1: (a) schematic diagram and (b) energy band diagram of the (Al/ITO/BaSnO<sub>3</sub>/CH<sub>3</sub>NH<sub>3</sub>PbI<sub>3</sub>/Cu<sub>2</sub>O/Cu or Mo) heterojunction solar cell.

### 3.2 Effect of the thicknesses and carrier concentration of various layer on the cell performance

The development of PV device optimization is a continuous process. In order to make efficient solar cells, each layer (mainly three layers: ETM, LHM, and HTM layer) and the interface between the layers need to be optimized. In this work, the thickness and carrier concentration of the HTM, LHM, and ETM layers were optimized to improve the PV performance of the cell. The initial values of thicknesses and carrier concentration of the LHM (absorber) and ETM layers

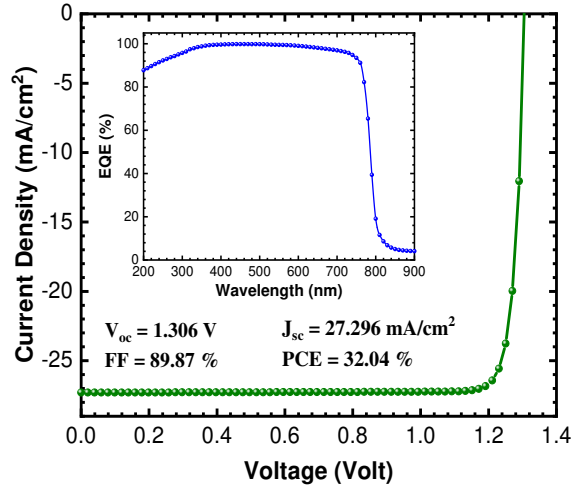


Fig. 2: J-V characteristics and EQE spectra of the  $\text{CH}_3\text{NH}_3\text{PbI}_3$ -based solar cells with the device structure of  $(\text{Al}/\text{ITO}/\text{BaSnO}_3/\text{CH}_3\text{NH}_3\text{PbI}_3/\text{Cu}_2\text{O}/\text{Cu}$  or  $\text{Mo})$ .

were set to 1000 nm and  $10^{17}$  cm<sup>-3</sup>, 100 nm, and  $10^{20}$  cm<sup>-3</sup>, respectively. An iterative simulation process was initiated to optimize HTM layer thickness and concentration. Then, using the obtained optimum HTM values, simulation was performed to calculate the new optimum ETM layer thickness and concentration. The process was repeated many times and the recorded results showed very good reproducibility. Finally, the optimized values of HTM and ETM layers were used to calculate the optimum thickness and acceptor concentration for the absorber layer.

### 3.2.1 Effect of $\text{Cu}_2\text{O}$ HTM layer thickness and carrier concentration

To understand the effect of  $\text{Cu}_2\text{O}$  HTM layer thickness and carrier concentration on the device performance, the thickness and concentration are varied from 75 nm to 175 nm and  $10^{17}$  to  $10^{21}$  cm<sup>-3</sup>, respectively. Single donor-type defects with a peak defect density of  $10^{16}$  eV<sup>-1</sup>cm<sup>-3</sup> was introduced in the HTM layer. It is found that the PV performance of the cell hardly changes within this thickness range (results not shown here), while the cell PV performance changes with the HTM layer carrier concentration, as shown in Fig. 3. In Fig. 3, the normalized values of all the PV performance parameters are plotted as a function of HTM layer carrier concentration. It can be seen from Fig. 3 that the newly modeled PSC shows almost constant PV performance up to the HTM layer carrier concentration of  $10^{19}$  cm<sup>-3</sup>. With the further increase of the HTM carrier concentration, the cell performance gradually increases. Finally, when the HTM layer carrier concentration exceeds  $10^{22}$  cm<sup>-3</sup>, the cell exhibits saturation behavior. In particular,  $V_{oc}$  increases as the carrier concentration of HTM rises from  $10^{19}$  to  $10^{22}$  cm<sup>-3</sup>, indicating a reduction in photo-generated charge carrier recombination within this concentration range. Moreover, the electric field at the HTM/LHM interface increases with the increase of HTM layer concentration, thereby improving the collection of photogenerated

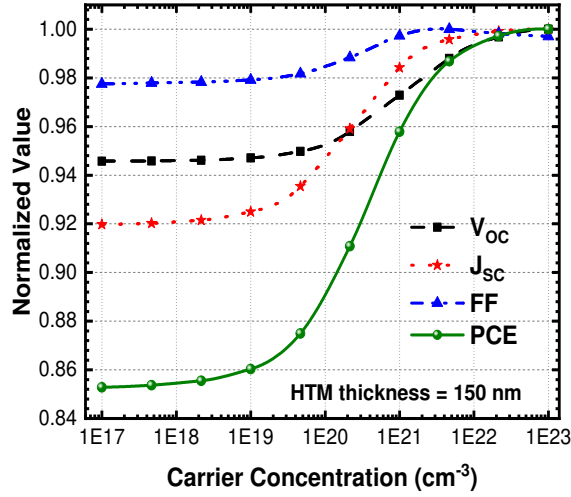


Fig. 3: Normalized values of all the PV performance parameters of PSC as a function of  $\text{Cu}_2\text{O}$  HTM layer carrier concentration.

carriers and enhancing  $J_{sc}$  and thus PCE. FF also increased slightly with the increase of HTM layer concentration, indicating that the series resistance of the device decreased. From this study, the enhanced PV performance of the device was found at the HTM layer carrier concentration of  $2.0 \times 10^{22} \text{ cm}^{-3}$  with a thickness of 150 nm.

### 3.2.2 Effect of $\text{BaSnO}_3$ ETM layer thickness and carrier concentration

The thickness of the  $\text{BaSnO}_3$  ETM layer should keep as possible as thinner than the other layers. Because a thinner ETM layer allows more photons to pass into the LHM layer and get absorbed. The simultaneous effect of ETM layer thickness and carrier concentration on cell performance was investigated, as it is important in terms of stability and performance of the device, and presented in Fig. 4. The carrier concentration and thickness was varied from  $10^{17}$  to  $10^{22} \text{ cm}^{-3}$  and 50 to 150 nm, respectively. Once again, single acceptor-type defects with a peak defect density of  $10^{16} \text{ eV}^{-1} \text{ cm}^{-3}$  was introduced into the ETM layer. It can be seen from Fig. 4 that all PV parameters (except  $J_{sc}$ ) of the cell exhibit similar behavior; at carrier concentration below  $10^{19} \text{ cm}^{-3}$ , PV parameters decline with increasing the thickness. This is due to increase of fractional absorption of incident light by ETM layer, increase of the bulk and surface recombination and increase in series resistance of the device [62]. However, enhanced PV performance is observed and one can hardly find any dependency on the PV parameters with the thickness when the carrier concentration is greater than  $10^{19} \text{ cm}^{-3}$ . This improvement of the PV performance of the device can be ascribed to the decrease of recombination of the minority charge carrier and series resistance with the increase of ETM layer carrier concentration. In contrast, the contour area for the highest  $J_{sc}$  extends in the thicker and highest concentration region (top-right). In this study, a maximum

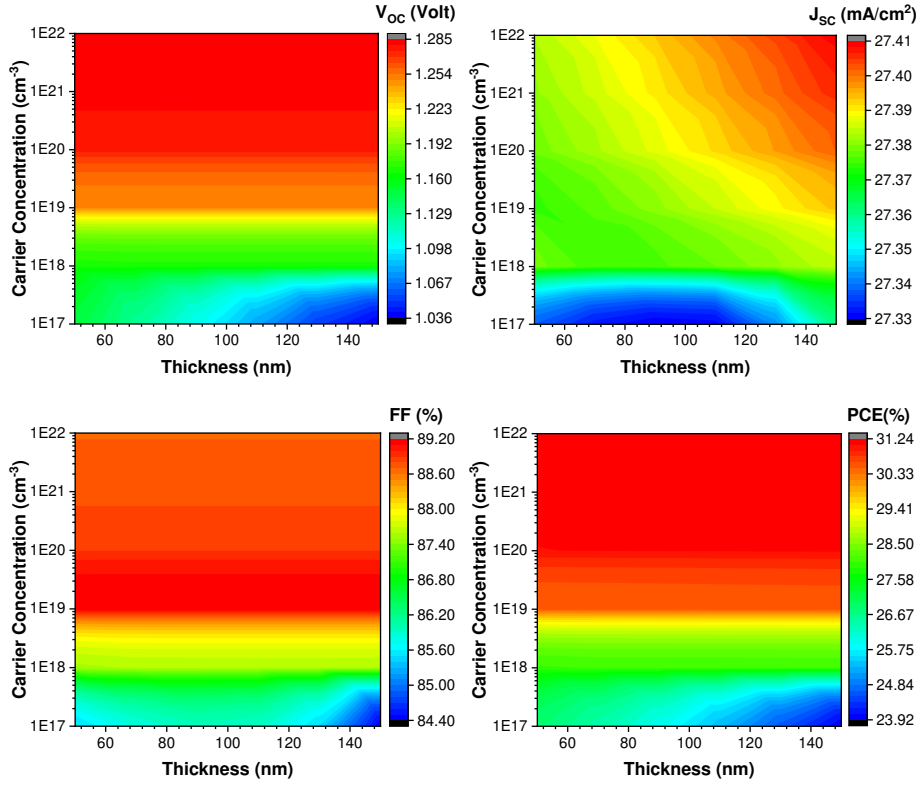


Fig. 4: Variation of PV performance parameters of PSC due to BaSnO<sub>3</sub> ETM layer thickness and carrier concentration.

PCE of 31.24% was observed at the ETM layer thickness of 100 nm and carrier concentration of  $> 10^{20}$  cm<sup>-3</sup>.

### 3.2.3 Effect of CH<sub>3</sub>NH<sub>3</sub>PbI<sub>3</sub> LHM layer thickness and carrier concentration

The spectral response of PV devices firmly relies on the thickness and carrier concentration of the LHM layer, which plays a significant role in determining the efficiency of the device. The LHM layer thickness and carrier concentration are the key choices for structuring the TFSCs, as it is generally influencing the photo-generated excitons and charge carrier extraction. Therefore, the optimization of the carrier concentration and thickness of the LHM layer is crucial in achieving optimum cell performance. The concurrent effect of the LHM layer carrier concentration and thickness on the PV performance of the novel (Al/ITO/BaSnO<sub>3</sub>/CH<sub>3</sub>NH<sub>3</sub>PbI<sub>3</sub>/Cu<sub>2</sub>O/Cu or Mo) heterojunction PSC was investigated, as shown in Fig. 5. In this simulation, single donor-type defects with a peak defect density of  $10^{15}$  eV<sup>-1</sup>cm<sup>-3</sup> was introduced in the LHM layer and the thickness and acceptor concentration of the LHM layer were varied from 400 to 1150 nm and  $10^{15}$  to  $10^{20}$  cm<sup>-3</sup>, respectively. As observed in Fig. 5, the changes in the thickness of the

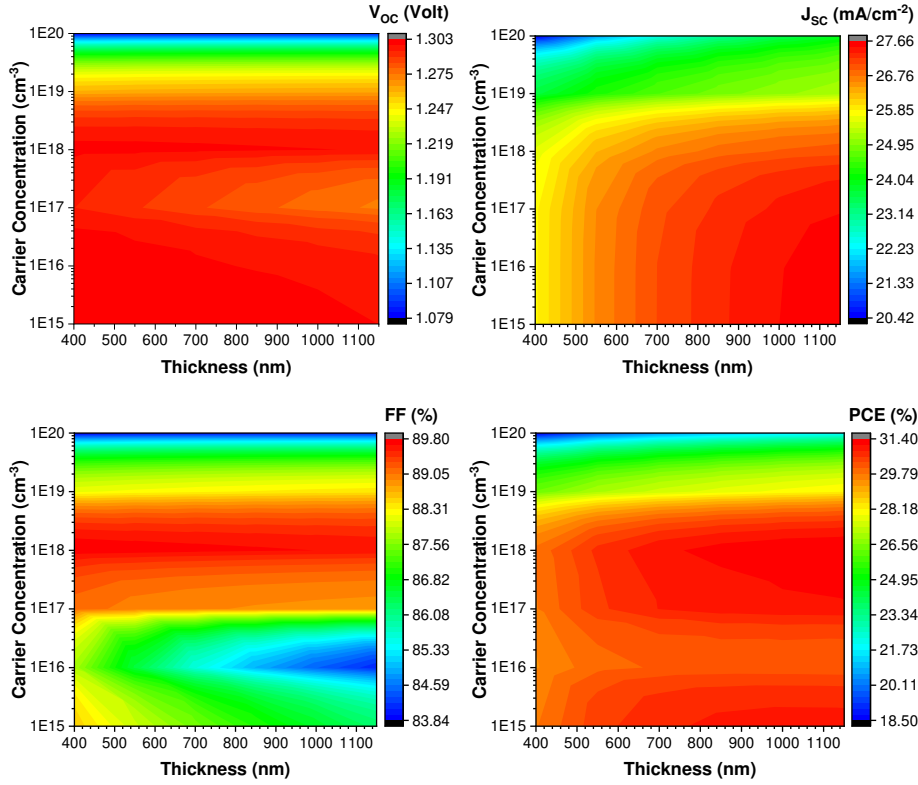


Fig. 5: Concurrent effect of thickness and acceptor concentration of  $\text{CH}_3\text{NH}_3\text{PbI}_3$  LHM layer on the performance of PSC.

LHM layer have little impact on  $V_{oc}$ . On the other hand, an increase in the acceptor concentration of the LHM layer from  $10^{15}$  to  $10^{20}$   $\text{cm}^{-3}$  causes a significant improvement in  $V_{oc}$  from 1.08 V to 1.3 V. This is attributed to the decrease in reverse saturation current as the carrier concentration increases, thereby increasing  $V_{oc}$ . The increased thickness helps to absorb more photons of longer wavelength, thereby increasing the current density, as it is seen in Fig. 5. The LHM layer carrier concentration mainly affects the lifetime of photogenerated electrons and depletion layer width at the interface, which in turn plays a major role in determining the photocurrent density. As the carrier concentration increases, the lifetime of photo-generated electrons and the width of the depletion layer are reduced, which leads to inefficient carrier collections at the interface, and therefore,  $J_{sc}$  is reduced. It is seen from Fig. 5 that the highest  $J_{sc}$  contour area exists in the area where the thickness of the LHM layer is the largest and the acceptor concentration is the lowest (bottom right). At lower acceptor concentration ( $< 10^{17}$   $\text{cm}^{-3}$ ), the FF slightly decreased with LHM layer thickness, which is due to the increase of series resistance of the device. The optimal FF for this kind of cells, which is almost independent of the thickness of the LHM layer, is found in the range of the accep-

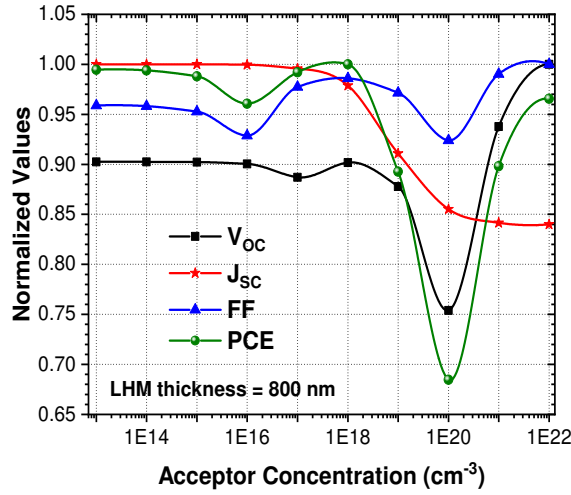


Fig. 6: Normalized values of all PV performance parameters of the PSC as a function of acceptor concentration of the LHM layer.

tor carrier concentration of  $10^{17}$  to  $10^{19}$   $\text{cm}^{-3}$ . According to this study, when the carrier concentration of the LHM layer is  $10^{18}$   $\text{cm}^{-3}$  and the thickness is 800 nm, the maximum PCE is found to be 31.40%.

It should be noted that the PV performance of the cell degraded at higher LHM layer carrier concentration, as all PV performance parameters of the cell turn down at the onset of the carrier concentration  $10^{18}$   $\text{cm}^{-3}$  of the LHM layer (see in Fig. 5). This effect can even be clearly seen in Fig. 6, where the normalized values of all PV parameters are plotted as a function of acceptor concentration of the LHM layer, keeping the constant LHM layer thickness of 800 nm. During this changeover, the values of all PV parameters show a sharp change from higher to a much lower value. This can be explained by the ETM and LHM layer doping levels. According to A. Niemegeers et al. [63], when the acceptor concentration of the LHM layer remains less than the donor concentration of the ETM layer, the defect state of the LHM/ETM interface is completely occupied by electrons and acts as a hole trap. However, when the acceptor density of the LHM layer exceeds the donor density of the ETM layer, most of the defect states in the LHM/ETM interface are occupied by holes, which act as electron traps in the interface area. These electron traps severely reduce the flow of electrons from the junction to the front electrode through the huge interface recombination, thereby reducing the overall cell performance. According to the semiconductor theory, as the acceptor doping concentration in the p-type absorber layer increases, the acceptor energy levels merge with the valance band, so that the Fermi energy lies within the band, thereby losing semiconducting properties and showing metallic behavior like degenerative semiconductors. Moreover, at higher carrier concentration level, the dominant impurity scattering also degrade the conductivity of the semiconductors. The observed transition of the overall cell performance can also be explained by the Mott transition theory [64]. Therefore, it can be concluded that when the

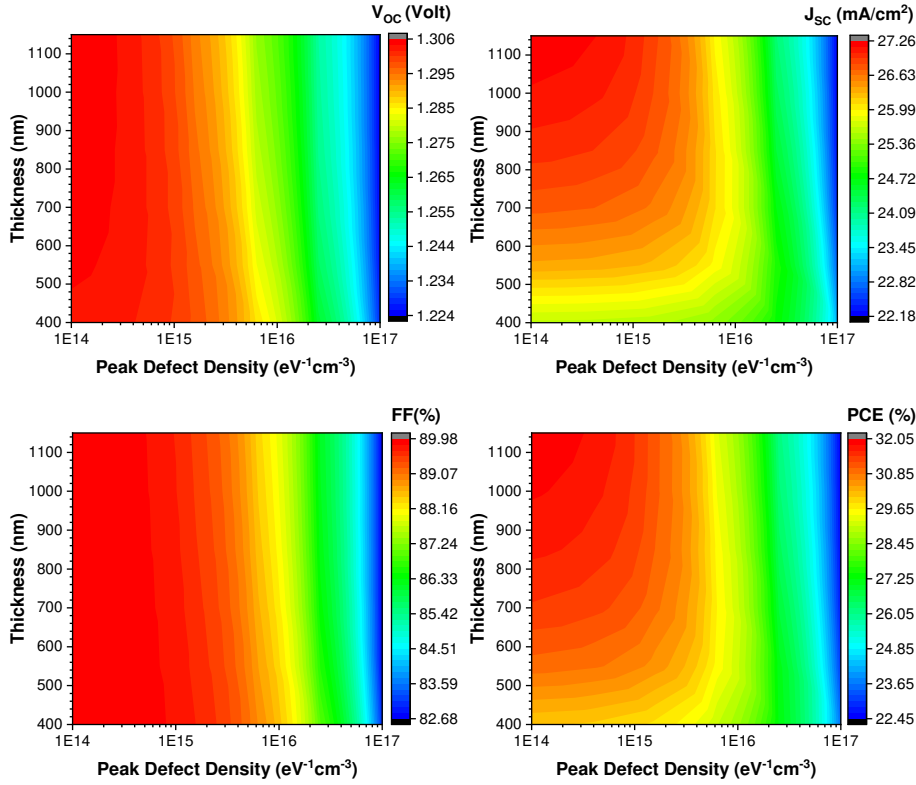


Fig. 7: Contour graphs of PSC performance parameters dependency on of  $\text{CH}_3\text{NH}_3\text{PbI}_3$  LHM layer defect density and thickness.

acceptor concentration of LHM layer does not exceed  $10^{18} \text{ cm}^{-3}$  and the thickness of the LHM layer is 800 nm, the device can produce the maximum PCE.

### 3.3 The impact of bulk defect density of $\text{CH}_3\text{NH}_3\text{PbI}_3$ LHM layer on device performance

As the photoelectrons generated in the LHM layer recombine in the LHM layer and at the interface, the density and nature of defects in the LHM layer play a crucial role in determining the performance of the PSCs. According to literature, the existing defects energy levels in the perovskite material can suitably be described by Gaussian distribution [65]. In this work, we used single-donor type bulk defects with Gaussian energetic distribution in p-type LHM layer. The LHM layer peak defect density was varied from  $10^{14}$  to  $10^{17} \text{ eV}^{-1}\text{cm}^{-3}$  taking a constant peak defect density of  $10^{16} \text{ eV}^{-1}\text{cm}^{-3}$  for all other layers. Fig. 7 presents the simultaneous effect of defects density and thickness of the LHM layer on the solar cell PV performance.

Varying peak defect density of the LHM layer from  $10^{14}$  to  $10^{17}$   $\text{eV}^{-1}\text{cm}^{-3}$ , the PCE of the PSC reduces from 32.05% to 22.45%, therefore, the device performance depends largely on the defect density of the LHM layer. It is observed from Fig. 7 that the  $V_{oc}$  is almost independent on the LHM layer thickness, while it changes from 1.3 V to 1.22 V as the peak defect density of the LHM layer is varied from  $10^{14}$  to  $10^{17}$   $\text{eV}^{-1}\text{cm}^{-3}$ . In contrast, the  $J_{sc}$  shows the highest value of 27.26  $\text{mA}/\text{cm}^2$  at thickness and peak defect density of greater than 1000 nm and less than  $10^{15}$   $\text{eV}^{-1}\text{cm}^{-3}$ , respectively. The decrease in thickness, as well as the increase of peak defect density causes a drop in the  $J_{sc}$  value. The highest contour area of the  $J_{sc}$  is in the upper left corner of the graph, where the thickness of the LHM layer and the peak defect density are the highest and lowest, respectively. FF depends on  $V_{oc}$  and the recombination processes in the depletion zone [66]. Therefore, compared with  $V_{oc}$ , the trend of FF is similar. The device exhibits FF of 89% at peak defect density of less than  $10^{15}$   $\text{eV}^{-1}\text{cm}^{-3}$ , which is not affected by the thickness. Conclusively, when the thickness is greater than 800 nm and the peak defect density is less than  $10^{15}$   $\text{eV}^{-1}\text{cm}^{-3}$ , the highest observed PCE is of about 32%. All the above findings suggest that the defect density of the LHM layer has an adverse effect on the performance of PSCs. However, we found that increasing the thickness of the LHM layer can weaken this problem.

### 3.4 Effect of working temperature and back contact metal work function on cell performance

Usually, in simulation studies and fabrication, the temperature of 300 K is chosen as the operating temperature where it is regarded as room temperature. In practice, the working temperature varies depending on the latitude, altitude, day of the year and time of day in a given location. Moreover, the performance of solar cells is affected by the operating temperature. **In this case, we varied the working temperature from 290K to 400K to achieve the actual behavior of the proposed PSC, and in this simulation, the optimized values of the variable parameters of the PSC obtained as before were used. The results of this simulation are shown in Fig. 8(a). Fig. 8(a) represents the normalized values of all the PV performance parameters of PSC as a function of working temperature.** It can be seen from Fig. 8(a) that the values of all PV parameters (except  $J_{sc}$ ) decrease monotonically with increasing the operating temperature, accompanied by a very small increment in  $J_{sc}$  value. At higher temperatures, the carrier concentration of the material, the mobility of the charge, the resistance, and the band gap of the material will be greatly affected, which will eventually change the PV parameters. In particular, the internal carrier recombination rate increases due to the increase of carrier concentration in semiconductor caused by higher operating temperature. As a matter of fact, the reverse saturation current increases, and finally the  $V_{oc}$  is reduced. A very small but definite increase in  $J_{sc}$  is attributed to the decrease of the band gap of semiconductor with increasing temperature. **In addition, at high temperature, the carrier mobility decreases due to the dominant lattice scattering, which deteriorates the PV performance of the solar cells. Therefore, the PV performance of the solar cells falls systematically as the temperature increases from 290K to 400K.** The temperature coefficient  $C_T$  ( $\%K^{-1}$ ) of PCE can be defined as

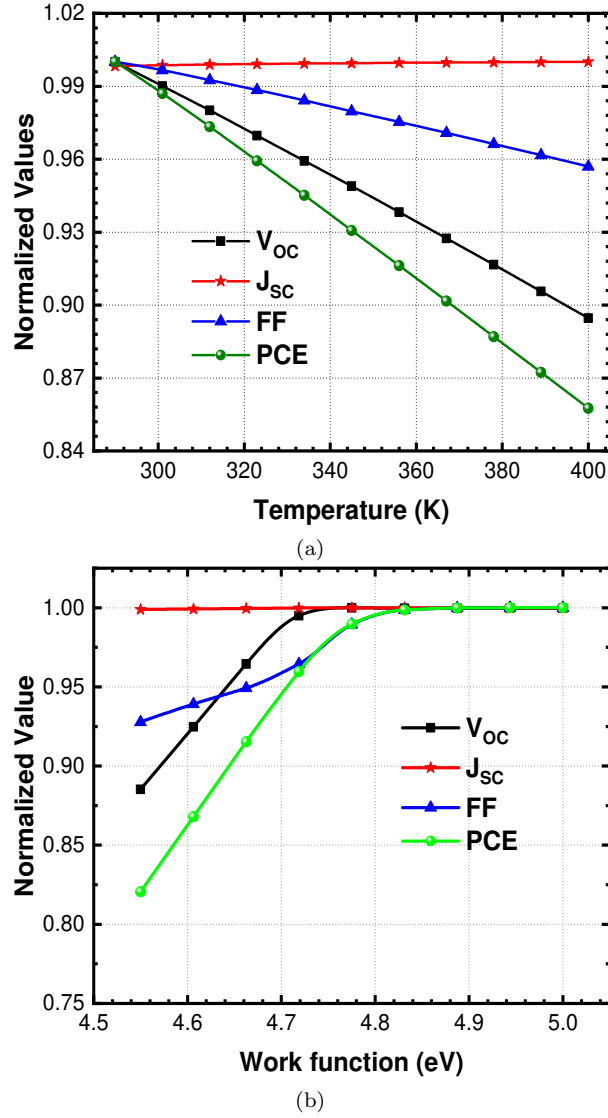


Fig. 8: Normalized values of all the PV performance parameters of the PSC as a function of (a) working temperature (b) back-contact metal work function.

the formula below under standard test conditions (STC)[15,67]

$$C_T = \left( \frac{1}{\eta_{STC}} \frac{d\eta_T}{dT} \times 100 \right) \quad (1)$$

where,  $\eta_{STC}$  is the cell efficiency at STC (298 K) and  $\eta_T$  is the efficiency at any temperature  $T$ . Using the equation (1), it is found that the temperature coefficient of PCE of the cell is only  $-0.112 \%K^{-1}$ , indicating very good PV performance stability at high temperature.

To investigate systemically the influence of the back-contact metal work function (WF) on the cell performance, its value was changed in the range from 4.55 to 5.0 eV in the simulation, and results are illustrated in Fig. 8(b). As shown in the figure,  $J_{sc}$  is less affected by the back-contact metal WF, however, by increasing the back-contact metal WF, an important improvement of the cell performance is observed. The results show that within a certain range from 4.55 to 4.85 eV, as the back electrode WF increases, the PCE,  $V_{oc}$ , and FF gradually increase and above the critical value of the metal WF (4.85 eV), these parameters indicate saturation behavior. For the higher values of back-contact metal WF, the barrier height relative to the Fermi level for majority charge carriers decreases, which means that the back-contacts become more ohmic, exhibits non-rectifying behavior, and allow easy carrier transport. Thus, the cell performance is enhanced. According to this study, we recommend using Cu (111) with a WF of 4.94 eV or Mo (110) with a WF of 4.95 eV as the back-contact materials in order to get a high-efficiency mark in this system.

#### 4 Conclusions

In this contribution, high-performance planar heterojunction perovskite ( $\text{CH}_3\text{NH}_3\text{PbI}_3$ ) solar cells with the novel device configuration of (Al/ITO/BaSnO<sub>3</sub>/CH<sub>3</sub>NH<sub>3</sub> PbI<sub>3</sub>/Cu<sub>2</sub>O/(Cu or Mo)) is implemented and investigated by SCAPS-1D. We have demonstrated that the role of BaSnO<sub>3</sub> as an electron transport material (ETM) and Cu<sub>2</sub>O as a hole transport material (HTM) are important in terms of device performance and stability. Using simulation software, different design strategies and factors such as thickness, carrier concentration of different layers, defect density of LHM layer, and back-contact metal WF have investigated. By optimizing the device parameters, we have achieved a simulated PCE of 32.0% with  $V_{oc} = 1.30$  V,  $J_{sc} = 27.26$  mA/cm<sup>2</sup>, and FF = 89% under AM1.5G illumination. In this simulation, it is suggested to provide the LHM, ETM and HTM layer with a thickness of 800 nm, 100 nm and 150 nm, respectively, and carrier concentration of  $10^{18}$  cm<sup>-3</sup>,  $10^{20}$  cm<sup>-3</sup> and  $2.0 \times 10^{22}$  cm<sup>-3</sup>, respectively, for optimum performance of the cell. The bulk defect density of the LHM layer has an adverse effect on the performance of the PSC, but in order to obtain the best performance, it should be controlled below  $10^{15}$  cm<sup>-3</sup>. This study also revealed that WF of back metal contact has a significant impact on cell performance and Cu (111) with WF of 4.94 eV or Mo with WF of 4.95 eV can be used as back-contact material to obtain better performance.

#### Declaration:

##### Funding

No funding was received for conducting this study

##### Conflict of Interest

The author declares no known competing financial interests or personal relationships that could have appeared to influence the work reported in this paper.

**Acknowledgements** The authors gratefully acknowledge Prof. Marc Burgelman, University of Gent, Belgium, for providing SCAPS 1-D simulation software.

## References

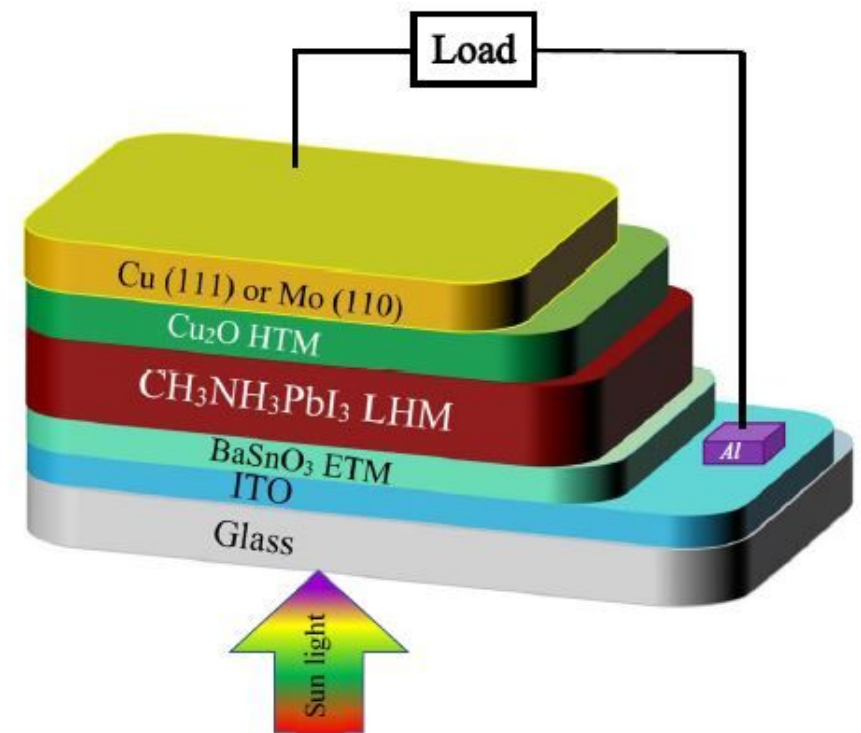
1. K. P. Bhandari, R. J. Ellingson: An overview of hybrid organic–inorganic metal halide perovskite solar cells *in: A Comprehensive Guide to Solar Energy Systems, Elsevier* pp. 233 – 254 (2018)
2. K. P. Bhandari, J. M. Collier, R. J. Ellingson, and D. S. Apul: Energy payback time (EPBT) and energy return on energy invested (EROI) of solar photovoltaic systems: A systematic review and meta-analysis, *Renewable and Sustainable Energy Reviews* 47, 133 – 141 (2015)
3. A. Polman, M. Knight, E. C. Garnett, B. Ehrler, and W. C. Sinke: 2016 Photovoltaic materials: Present efficiencies and future challenges, *Science* 352 aad4424 – aad4424, (2016)
4. M. Green, E. Dunlop, J. Hohl-Ebinger, M. Yoshita, N. Kopidakis, and X. Hao: Solar cell efficiency tables (version 57), *Progress in Photovoltaics: Research and Applications*, 29, 3 – 15 (2020)
5. C. Candelise, M. Winkler, and R. Gross: Implications for CdTe and CIGS technologies production costs of indium and tellurium scarcity, *Progress in Photovoltaics: Research and Applications*, 20 816 – 831, (2012).
6. B. A. Andersson: Materials availability for large-scale thin-film photovoltaics, *Progress in Photovoltaics: Research and Applications*, 8, 61 – 76 (2000)
7. B. A. Schubert, I. M. Kotschau, S. Cinque, H. W. Schock: An economic approach to evaluate the range of coverage of indium and its impact on indium based thin-film solar cells recent results of  $\text{Cu}_2\text{ZnSnS}_4$  (CZTS) based solar cells, *in: Proceedings of the 23rd EU-PVSEC, Valencia, 7788-3792* (2008)
8. K. Zweibel: The terawatt challenge for thin film photovoltaics, *in: J. Poortmans, V. Arkhipov (Eds.), Thin Film Solar Cells: Fabrication, Characterization and Applications, 427-462, John Wiley & Sons Ltd. (2006)*
9. Gregory Phipps, Claire Mikolajczak, and Terry Guckes: Indium and gallium: long-term supply, *Renewable Energy Focus*, 9, 56–59 (2008)
10. Kentaro Ito and Tatsuo Nakazawa: Electrical and optical properties of stannite-type quaternary semiconductor thin films. *Japanese Journal of Applied Physics*, 27 (Part 1, No. 11), 2094–2097 (1988)
11. Hironori Katagiri, Nobuyuki Sasaguchi, Shima Hando, Suguro Hoshino, Jiro Ohashi, and Takaharu Yokota: Preparation and evaluation of  $\text{Cu}_2\text{ZnSnS}_4$  thin films by sulfurization of e-b evaporated precursors, *Solar Energy Materials and Solar Cells*, 49, 407–414 (1997)
12. Wei Wang, Mark T. Winkler, Oki Gunawan, Tayfun Gokmen, Teodor K. Todorov, Yu Zhu, and David B. Mitzi: Device characteristics of CZTSSe thin-film solar cells with 12.6% efficiency. *Advanced Energy Materials*, 4, 1301465 (2013)
13. Jeehwan Kim, Homare Hiroi, Teodor K. Todorov, Oki Gunawan, Masaru Kuwahara, Tayfun Gokmen, Dhruv Nair, Marinus Hopstaken, Byungha Shin, Yun Seog Lee, Wei Wang, Hiroki Sugimoto, and David B. Mitzi: High efficiency  $\text{Cu}_2\text{ZnSn}(\text{S},\text{Se})_4$  solar cells by applying a double  $\text{In}_2\text{S}_3/\text{CdS}$  emitter, *Advanced Materials*, 26, 7427–7431 (2014)
14. M. Atowar Rahman, Enhancing the photovoltaic performance of Cd-free  $\text{Cu}_2\text{ZnSnS}_4$  heterojunction solar cells using SnS HTL and  $\text{TiO}_2$  ETL, *Solar Energy*, 215, 64–76 (2021)
15. M. Atowar Rahman, Design and simulation of a high-performance Cd-free  $\text{Cu}_2\text{ZnSnSe}_3$  solar cells with SnS electron-blocking hole transportlayer and  $\text{TiO}_2$  electron transport layer by SCAPS-1D, *SN Applied Sciences*, 3, 253 (2021)
16. Nam-Gyn Park, Michael Gratzel, Tsutomu Miyasaka, Kai Zhu and Keith Emery: Towards stable and commercially available perovskite solar cells, *Nature Energy*, 1, 16152 (2016)
17. Julian Burschka, Norman Pellet, Soo-Jin Moon, Robin Humphry-Baker, Peng Gao, Mohammad K. Nazeeruddin, and Michael Gratzel: Sequential deposition as a route to high-performance perovskite sensitized solar cells, *Nature*, 499, 316–319 (2013)
18. [15] Dianyi Liu and Timothy L. Kelly: Perovskite solar cells with a planar heterojunction structure prepared using room-temperature solution processing techniques, *Nature Photonics*, 8, 133–138 (2013)
19. Jin Hyuck Heo, Sang Hyuk Im, Jun Hong Noh, Tarak N. Mandal, Choong-Sun Lim, Jeong Ah Chang, Yong Hui Lee, Hi jung Kim, Arpita Sarkar, Md. K. Nazeeruddin, Michael Gratzel, and Sang Il Seok: Efficient inorganic–organic hybrid heterojunction solar cells containing perovskite compound and polymeric hole conductors, *Nature Photonics*, 7, 486–491 (2013)
20. W. Nie, H. Tsai, R. Asadpour, J.-C. Blancon, A. J. Neukirch, G. Gupta, J. J. Crochet, M. Chhowalla, S. Tretiak, M. A. Alam, H.-L. Wang, and A. D. Mohite: High-efficiency solution-processed perovskite solar cells with millimeter-scale grains, *Science*, 347, 522–525 (2015)

21. Nam Joong Jeon, Jun Hong Noh, Young Chan Kim, Woon Seok Yang, Seungchan Ryu, and Sang Il Seok: Solvent engineering for high-performance inorganic-organic hybrid perovskite solar cells, *Nature Materials*, 13, 897–903 (2014)
22. Nam Joong Jeon, Jun Hong Noh, Woon Seok Yang, Young Chan Kim, Seungchan Ryu, Jangwon Seo, and Sang Il Seok: Compositional engineering of perovskite materials for high-performance solar cells, *Nature*, 517, 476–480 (2015)
23. Mingzhen Liu, Michael B. Johnston, and Henry J. Snaith: Efficient planar heterojunction perovskite solar cells by vapour deposition, *Nature*, 501, 395–398 (2013)
24. Best Research-Cell Efficiency Chart, National Renewable Energy Laboratory (NREL), Technical Report, (2020). URL:<https://www.nrel.gov/pv/cell-efficiency.html>.
25. William Shockley and Hans J. Queisser: Detailed balance limit of efficiency of p-n junction solar cells, *Journal of Applied Physics*, 32, 510–519 (1961)
26. Wanyi Nie, Jean-Christophe Blancon, Amanda J. Neukirch, Kannatassen Appavoo, Hsinhan Tsai, Manish Chhowalla, Muhammad A. Alam, Matthew Y. Sfeir, Claudine Katan, Jacky Even, Sergei Tretiak, Jared J. Crochet, Gautam Gupta, and Aditya D. Mohite: Light-activated photocurrent degradation and self-healing in perovskite solar cells, *Nature Communications*, 7, 11574 (2016)
27. A. Mei, X. Li, L. Liu, Z. Ku, T. Liu, Y. Rong, M. Xu, M. Hu, J. Chen, Y. Yang, M. Gratzel, and H. Han: A hole-conductor-free, fully printable mesoscopic perovskite solar cell with high stability, *Science*, 345, 295–298, (2014)
28. W. Qiu, T. Merckx, M. Jaysankar, C. Masse de la Huerta, L. Rakocevic, W. Zhang, U. W. Paetzold, R. Gehlhaar, L. Froyen, J. Poortmans, D. Cheyens, H. J. Snaith, and P. Heremans: Pinhole-free perovskite films for efficient solar modules, *Energy & Environmental Science*, 9, 484–489 (2016)
29. Thomas M. Brenner, David A. Egger, Leeor Kronik, Gary Hodes, and David Cahen: Hybrid organic-inorganic perovskites: low-cost semiconductors with intriguing charge-transport properties, *Nature Reviews Materials*, 1, 15007 (2016)
30. Takashi Minemoto and Masashi Murata: Theoretical analysis on effect of band offsets in perovskite solar cells. *Solar Energy Materials and Solar Cells*, 133, 8–14 (2015)
31. Emilio J. Juarez-Perez, Michael Wuler, Francisco Fabregat-Santiago, Kerstin Lakus-Wollny, Eric Mankel, Thomas Mayer, Wolfram Jaegermann, and Ivan Mora-Sero: Role of the selective contacts in the performance of lead halide perovskite solar cells. *The Journal of Physical Chemistry Letters*, 5, 680–685 (2014)
32. Wenzhe Li, Wei Zhang, Stephan Van Reenen, Rebecca J. Sutton, Jiandong Fan, Amir A. Haghighirad, Michael B. Johnston, Liduo Wang, and Henry J. Snaith: Enhanced UV-light stability of planar heterojunction perovskite solar cells with caesium bromide interface modification. *Energy & Environmental Science*, 9, 490–498 (2016)
33. Philip Schulz, Eran Edri, Saar Kirmayer, Gary Hodes, David Cahen, and Antoine Kahn: Interface energetics in organo-metal halide perovskite based photovoltaic cells, *Energy & Environmental Science*, 7, 1377 (2014)
34. Peng Gao, Michael Gratzel, and Mohammad K. Nazeeruddin: Organohalide lead perovskites for photovoltaic applications, *Energy Environ. Sci.*, 7, 2448–2463 (2014)
35. U. Bach, D. Lupo, P. Comte, J. E. Moser, F. Weissortel, J. Salbeck, H. Spreitzer, and M. Gratzel: Solid-state dye-sensitized mesoporous TiO<sub>2</sub> solar cells with high photon-to-electron conversion efficiencies, *Nature*, 395, 583–585 (1998)
36. Julian Burschka, Amalie Dualeh, Florian Kessler, Etienne Baranoff, Ngoc-Le Cevey-Ha, Chenyi Yi, Mohammad K. Nazeeruddin, and Michael Gratzel: Tris(2-(1h-pyrazol-1-yl)pyridine)cobalt(III) as p-type dopant for organic semiconductors and its application in highly efficient solid-state dye-sensitized solar cells, *Journal of the American Chemical Society*, 133, 18042–18045 (2011)
37. E. H. Jung, N. J. Jeon, E. Y. Park, C. S. Moon, T. J. Shin, T.-Y. Yang, J. H. Noh, J. Seo: Efficient, stable and scalable perovskite solar cells using poly(3-hexylthiophene), *Nature* 567, 511–515 (2019)
38. Haining Chen, Zhanhua Wei, Hexiang He, Xiaoli Zheng, Kam Sing Wong, and Shihe Yang: Solvent engineering boosts the efficiency of paintable carbon-based perovskite solar cells to beyond 14%. *Advanced Energy Materials*, 6, 1502087 (2016)
39. Jeffrey A. Christians, Raymond C. M. Fung, and Prashant V. Kamat: An inorganic hole conductor for organo-lead halide perovskite solar cells: improved hole conductivity with copper iodide, *Journal of the American Chemical Society*, 136, 758–764 (2013)
40. Seigo Ito, Soichiro Tanaka, Henri Vahlman, Hitoshi Nishino, Kyohei Manabe, and Peter Lund: Carbon-double-bond-free printed solar cells from TiO<sub>2</sub>/CH<sub>3</sub>NH<sub>3</sub>PbI<sub>3</sub>/CuSCN/Au: Structural control and photoaging effects, *ChemPhysChem*, 15, 1194–1200 (2014)

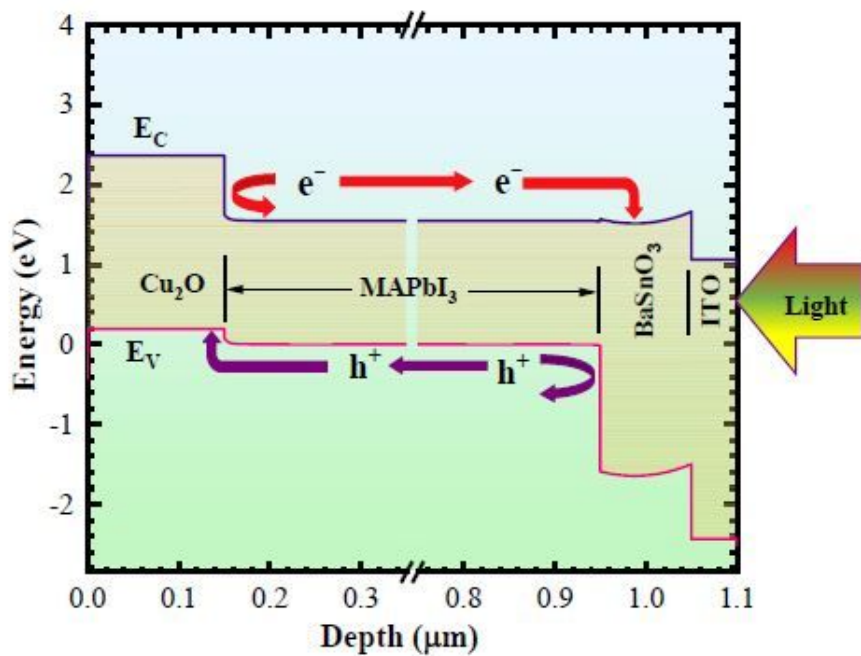
41. Mohammad I. Hossain, Fahhad H. Alharbi, and Nouar Tabet: Copper oxide as inorganic hole transport material for lead halide perovskite based solar cells, *Solar Energy*, 120, 370–380 (2015)
42. Khalid Mahmood, Saad Sarwar, and Muhammad Taqi Mehran: Current status of electron transport layers in perovskite solar cells: materials and properties, *RSC Advances*, 7, 17044–17062 (2017)
43. Jai Prakash, Arjun Singh, Govindasamy Sathiyam, Rahul Ranjan, Anand Singh, Ashish Garg, and Raju Kumar Gupta: Progress in tailoring perovskite based solar cells through compositional engineering: Materials properties, photovoltaic performance and critical issues, *Materials Today Energy*, 9, 440–486 (2018)
44. Suresh Gubbala, Vidhya Chakrapani, Vivekanand Kumar, and Mahendra K. Sunkara: Band-edge engineered hybrid structures for dye-sensitized solar cells based on SnO<sub>2</sub>nanowires, *Advanced Functional Materials*, 18, 2411–2418 (2008)
45. Dae-Yong Son, Jeong-Hyeok Im, Hui-Seon Kim, and Nam-Gyu Park: 11% efficient perovskite solar cell based on ZnO nanorods: An effective charge collection system. *The Journal of Physical Chemistry C*, 118, 16567–16573 (2014)
46. Rong Zhang, Chengbin Fei, Bo Li, Haoyu Fu, Jianjun Tian, and Guozhong Cao: Continuous size tuning of monodispersed ZnO nanoparticles and its size effect on the performance of perovskite solar cells, *ACS Applied Materials & Interfaces*, 9, 9785–9794 (2017)
47. Juan Pablo Correa Baena, Ludmilla Steier, Wolfgang Tress, Michael Saliba, Stefanie Neutzner, Taisuke Matsui, Fabrizio Giordano, T. Jesper Jacobsson, Ajay Ram Srimath Kandada, Shaik M. Zakeeruddin, Annamaria Petrozza, Antonio Abate, Mohammad Khaja Nazeeruddin, Michael Grätzel, and Anders Hagfeldt: Highly efficient planar perovskite solar cells through band alignment engineering. *Energy & Environmental Science*, 8, 2928–2934 (2015)
48. W. Chen, Y. Wu, Y. Yue, J. Liu, W. Zhang, X. Yang, H. Chen, E. Bi, I. Ashraful, M. Grätzel, and L. Han, Efficient and stable large-area perovskite solar cells with inorganic charge extraction layers, *Science*, 350, 944–948 (2015)
49. Liangzheng Zhu, Zhipeng Shao, Jiajiu Ye, Xuhui Zhang, Xu Pan, and Songyuan Dai: Mesoporous BaSnO<sub>3</sub> layer based perovskite solar cells, *Chemical Communications*, 52, 970–973 (2016).
50. Herbert B. Michaelson: The work function of the elements and its periodicity, *Journal of Applied Physics*, 48, 4729–4733 (1977)
51. M Burgelman, P Nollet, and S Degraeve: Modelling polycrystalline semiconductor solar cells, *Thin Solid Films*, 361-362, 527–532 (2000)
52. Wenhao Zhao, Wenli Zhou, and Xiangshui Miao: Numerical simulation of CZTS thin film solar cell, In 2012 7th IEEE International Conference on Nano/Micro Engineered and Molecular Systems (NEMS), Japan, pp 502-505 (2012)
53. C. Guillen and J. Herrero: Single-phase Cu<sub>2</sub>O and CuO thin films obtained by low-temperature oxidation processes, *Journal of Alloys and Compounds*, 737, 718–724 (2018)
54. Sang-Hoon Bae, Hongxiang Zhao, Yao-Tsung Hsieh, Lijian Zuo, Nicholas De Marco, You Seung Rim, Gang Li, and Yang Yang: Printable solar cells from advanced solution-processible materials, *Chem*, 1, 197–219 (2016)
55. Hyung Joon Kim, Useong Kim, Tai Hoon Kim, Jiyeon Kim, Hoon Min Kim, Byung-Gu Jeon, Woong-Jhae Lee, Hyo Sik Mun, Kwang Taek Hong, Jaejun Yu, Kookrin Char, and Kee Hoon Kim: Physical properties of transparent perovskite oxides (Ba,La)SnO<sub>3</sub> with high electrical mobility at room temperature, *Physical Review B*, 86, 165205 (2012)
56. N. M. Khusayfan and M. M. El-Nahass: Study of structure and electro-optical characteristics of indium tin oxide thin films, *Advances in Condensed Matter Physics*, 2013, 1–8 (2013)
57. R. Hulstrom, R. Bird, and C. Riordan: Spectral solar irradiance data sets for selected terrestrial conditions, *Solar Cells*, 15, 365–391 (1985)
58. William Nunn, Abhinav Prakash, Arghya Bhowmik, Ryan Haislmaier, Jin Yue, Juan Maria Garcia Lastra, and Bharat Jalan: Frequency- and temperature-dependent dielectric response in hybrid molecular beam epitaxy-grown BaSnO<sub>3</sub> films, *APL MATERIALS* 6, 066107 (2018)
59. Paulina Sawicka-Chudy, Maciej Sibiński, Grzegorz Wisz, Elżbieta Rybak-Wilusz and Marian Cholewa: Numerical analysis and optimization of Cu<sub>2</sub>O/TiO<sub>2</sub>, CuO/TiO<sub>2</sub>, heterojunction solar cells using SCAPS, *IOP Conf. Series: Journal of Physics: Conf. Series*, 1033, 012002 (2018)
60. Ali Hajjiah, Hussein Badran, Ishac Kandas and Nader Shehata: Perovskite Solar Cell with Added Gold/Silver Nanoparticles: Enhanced Optical and Electrical Characteristics, *Energies*, 13, 3854 (2020)

61. T. Minemoto, T. Matsui, H. Takakura, Y. Hamakawa, T. Negami, Y. Hashimoto, T. enoyama, and M. Kitagawa, Theoretical analysis of the effect of conduction band offset of window/CIS layers on performance of CIS solar cells using device simulation, *Sol. Energy Mater. Sol. Cells*, 67, 83 (2001).
62. Thakur U K, Kisslinger R and Shankar K, One-Dimensional Electron Transport Layers for Perovskite Solar Cells, *Nanomaterials*, 7, 95 (2017).
63. Alex Niemegeers, M. Burgelman, Alexis De Vos, On the CdS/CuInSe<sub>2</sub> conduction band discontinuity, *Appl. Phys. Lett.*, 67, 843-845 (1995)
64. N. F. Mott, Metal-insulator transition, *Rev. Mod. Phys.*, 40, 677 (1968)
65. W. J. Yin, T. T. Shi, and Y. T. Yan: Unusual defect physics in CH<sub>3</sub>NH<sub>3</sub>PbI<sub>3</sub> perovskite solar cell absorber, *Appl. Phys. Lett.*, vol. 104, no. 6, pp. 063903-1–063903-4, Feb. 2014
66. Hossain E. S, Chelvanathan P, Shahahmadi S. A, Sopian K, Bais B, and Amin N: Performance assessment of Cu<sub>2</sub>SnS<sub>3</sub> (CTS) based thin film solar cells by AMPS-1D, *Curr. Appl. Phys.*, 18, 79–89 (2018)
67. Y. J. Ren, S. H. Lie, Z. Lang, H. H. Bin, Z. N. Gen, D. X. Hua, and Y. Q. Ming:  $\beta$ -FeSi<sub>2</sub> as the bottom absorber of triple-junction thin-film solar cells: A numerical study, *Chin. Phys. B*, 23, 038801 (2014)

# Figures



(a)



(b)

Figure 1

(a) schematic diagram and (b) energy band diagram of the (Al/ITO/BaSnO<sub>3</sub>/CH<sub>3</sub>NH<sub>3</sub>PbI<sub>3</sub>/Cu<sub>2</sub>O/Cu or Mo) heterojunction solar cell.

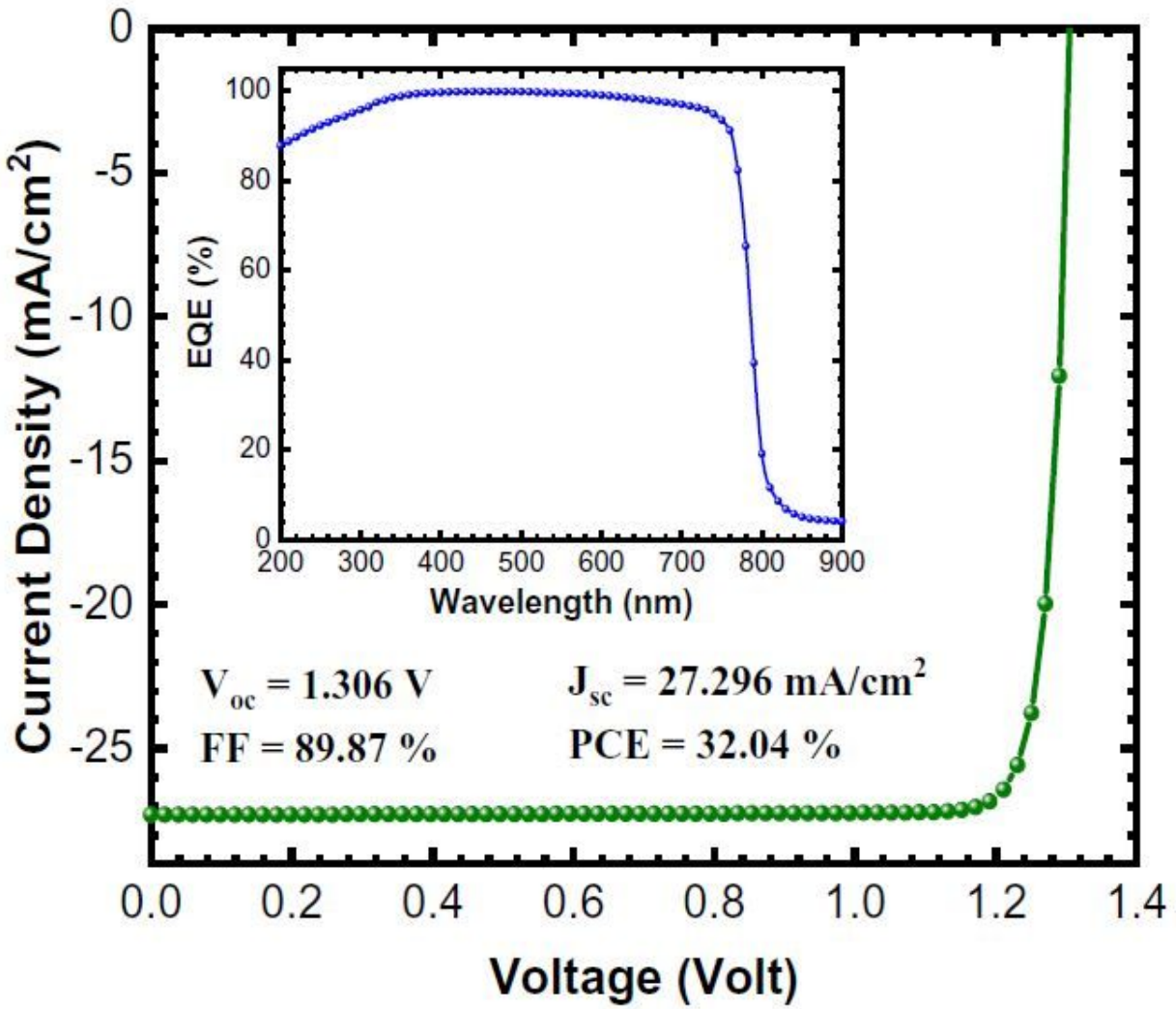


Figure 2

J-V characteristics and EQE spectra of the CH<sub>3</sub>NH<sub>3</sub>PbI<sub>3</sub>-based solar cells with the device structure of (Al/ITO/BaSnO<sub>3</sub>/CH<sub>3</sub>NH<sub>3</sub>PbI<sub>3</sub>/Cu<sub>2</sub>O/Cu or Mo).

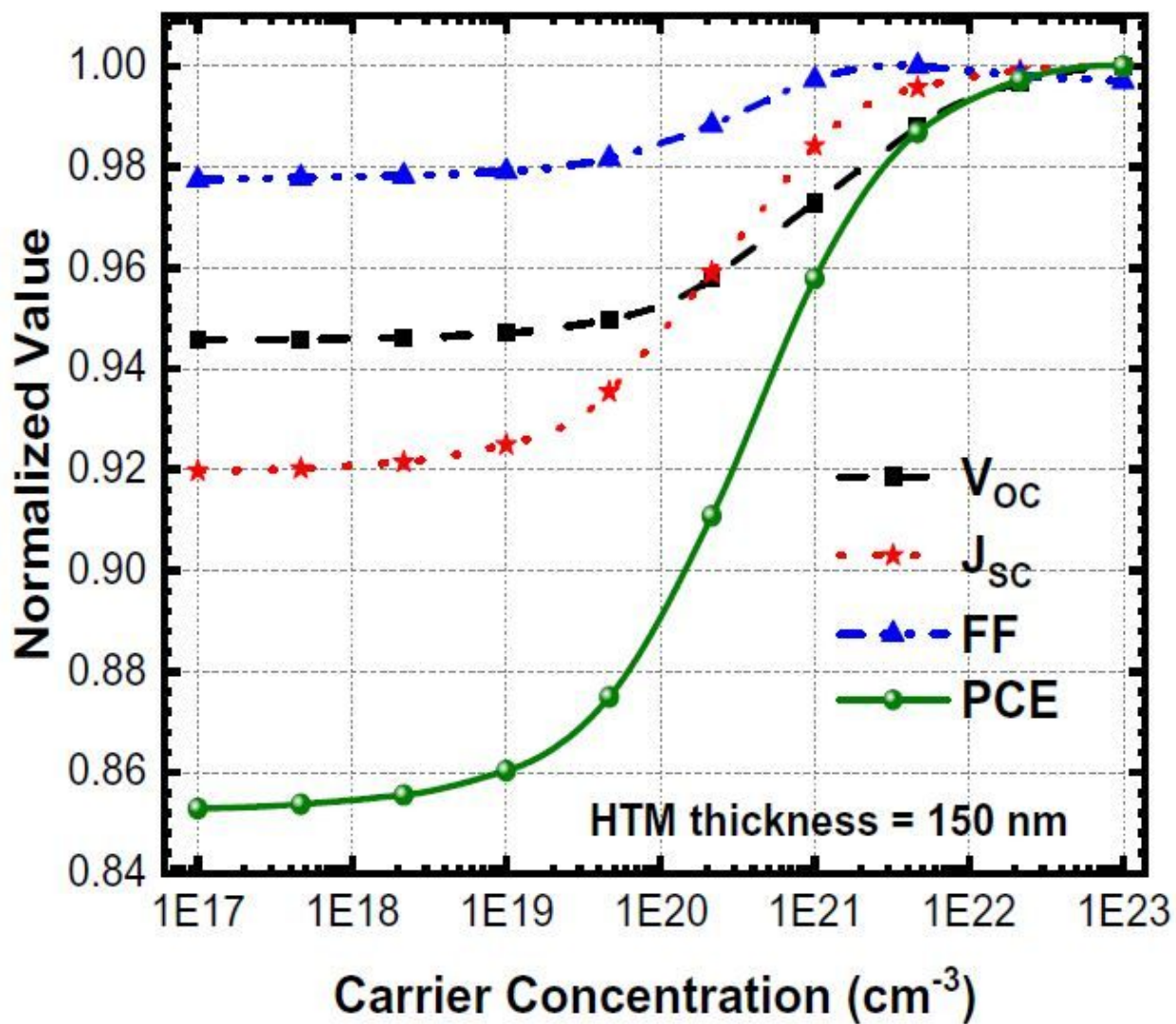
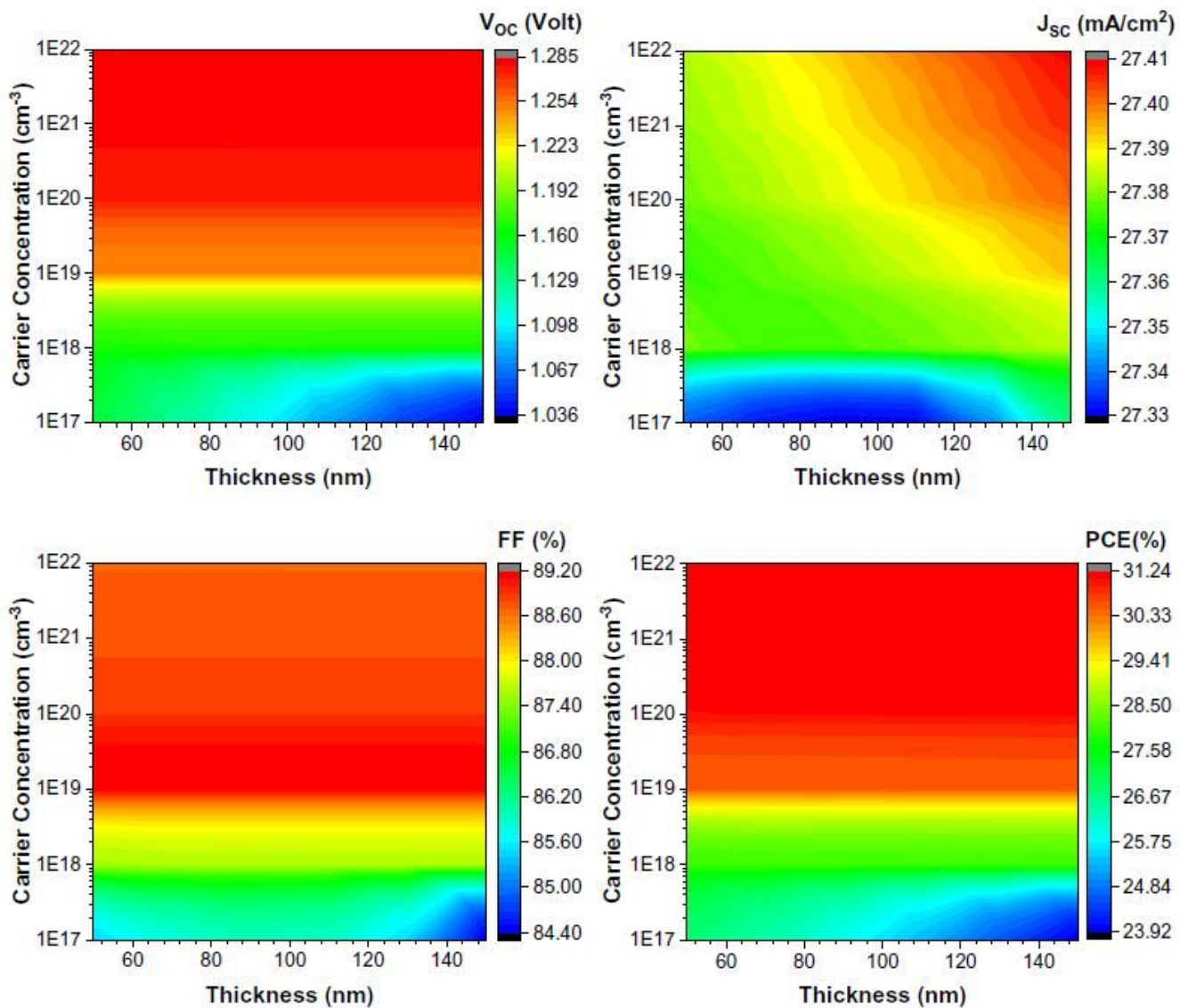


Figure 3

Normalized values of all the PV performance parameters of PSC as a function of Cu<sub>2</sub>O HTM layer carrier concentration.



**Figure 4**

Variation of PV performance parameters of PSC due to BaSnO<sub>3</sub> ETM layer thickness and carrier concentration.

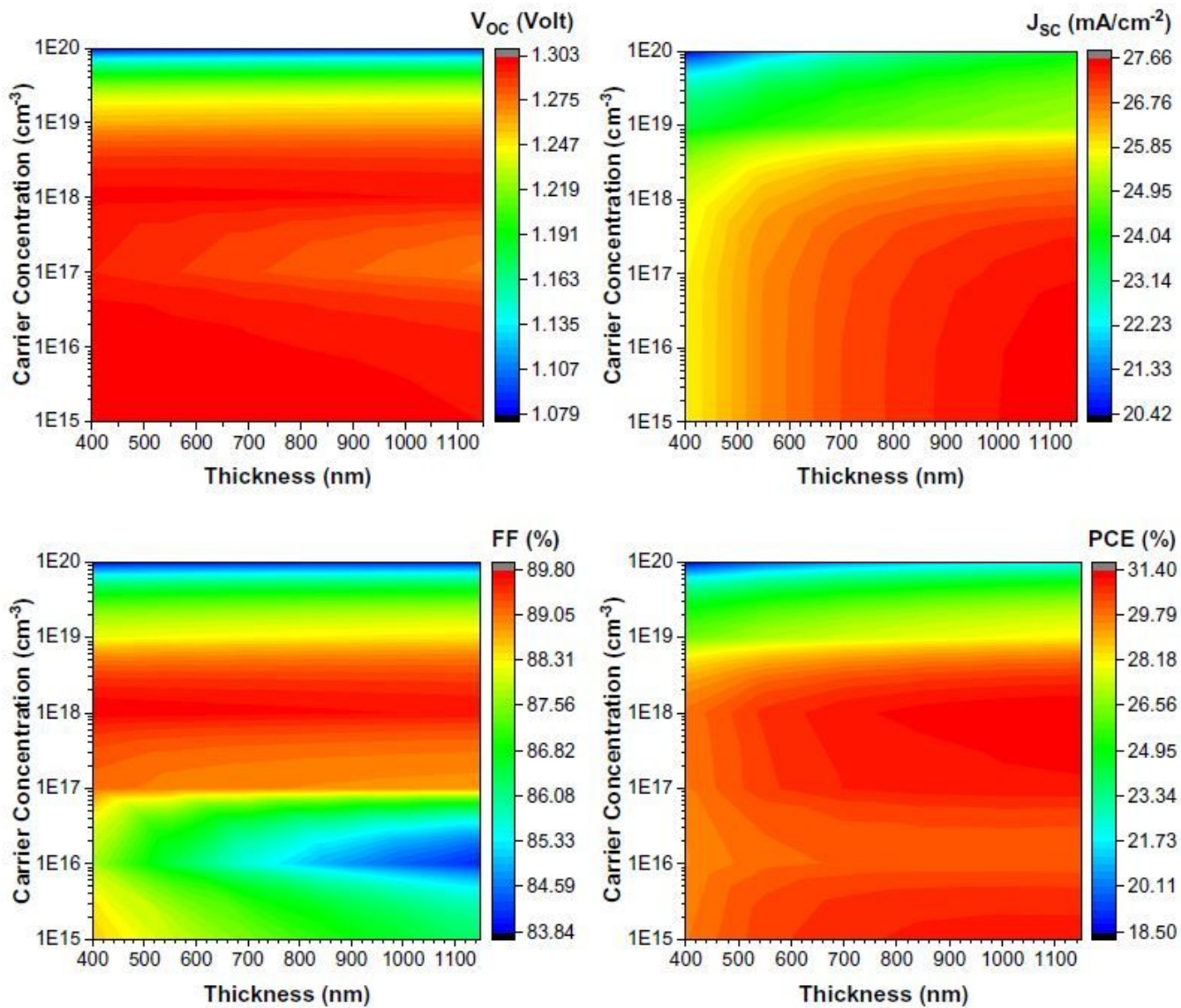


**Figure 5**

Concurrent effect of thickness and acceptor concentration of CH<sub>3</sub>NH<sub>3</sub>PbI<sub>3</sub> LHM layer on the performance of PSC.

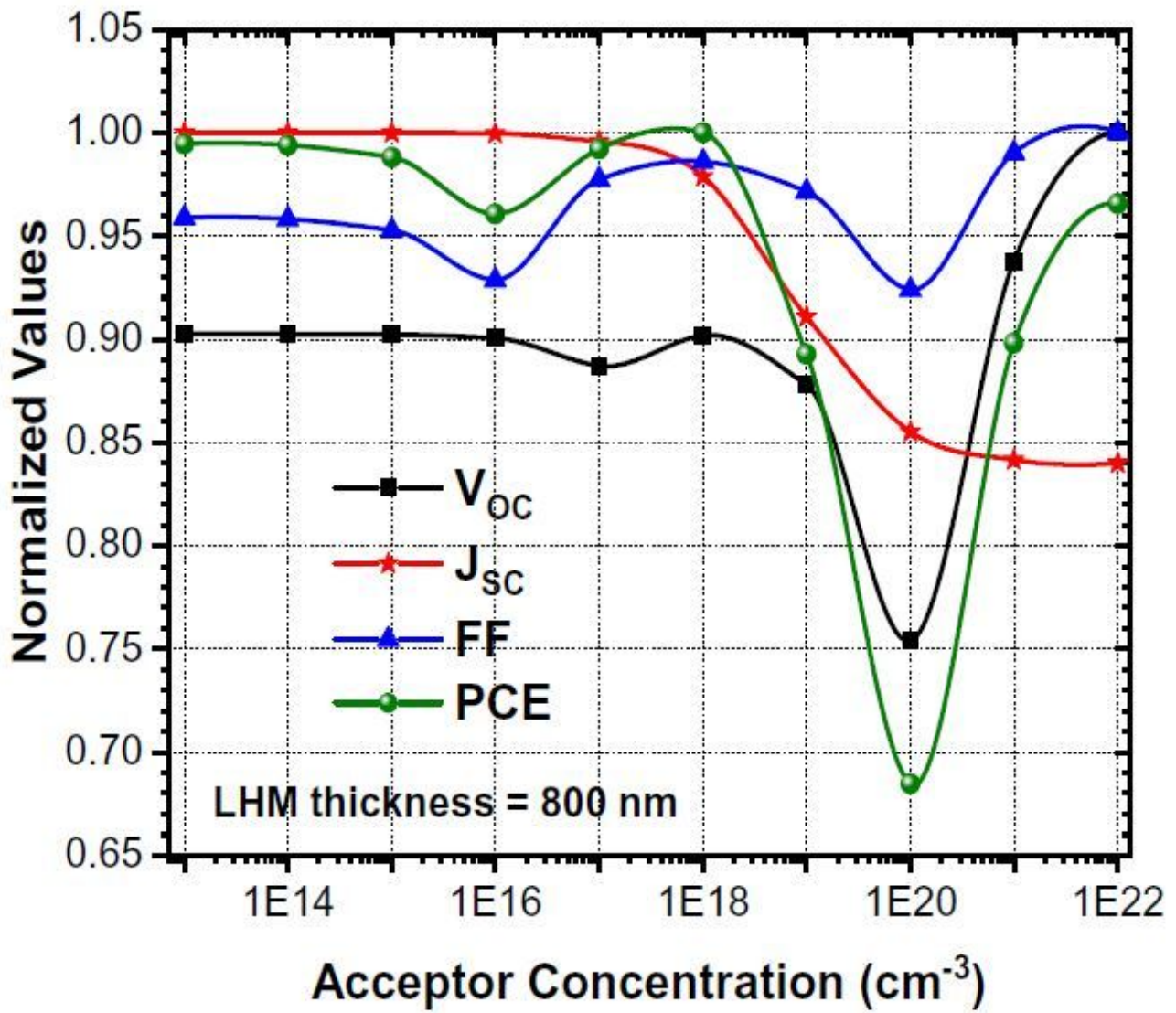
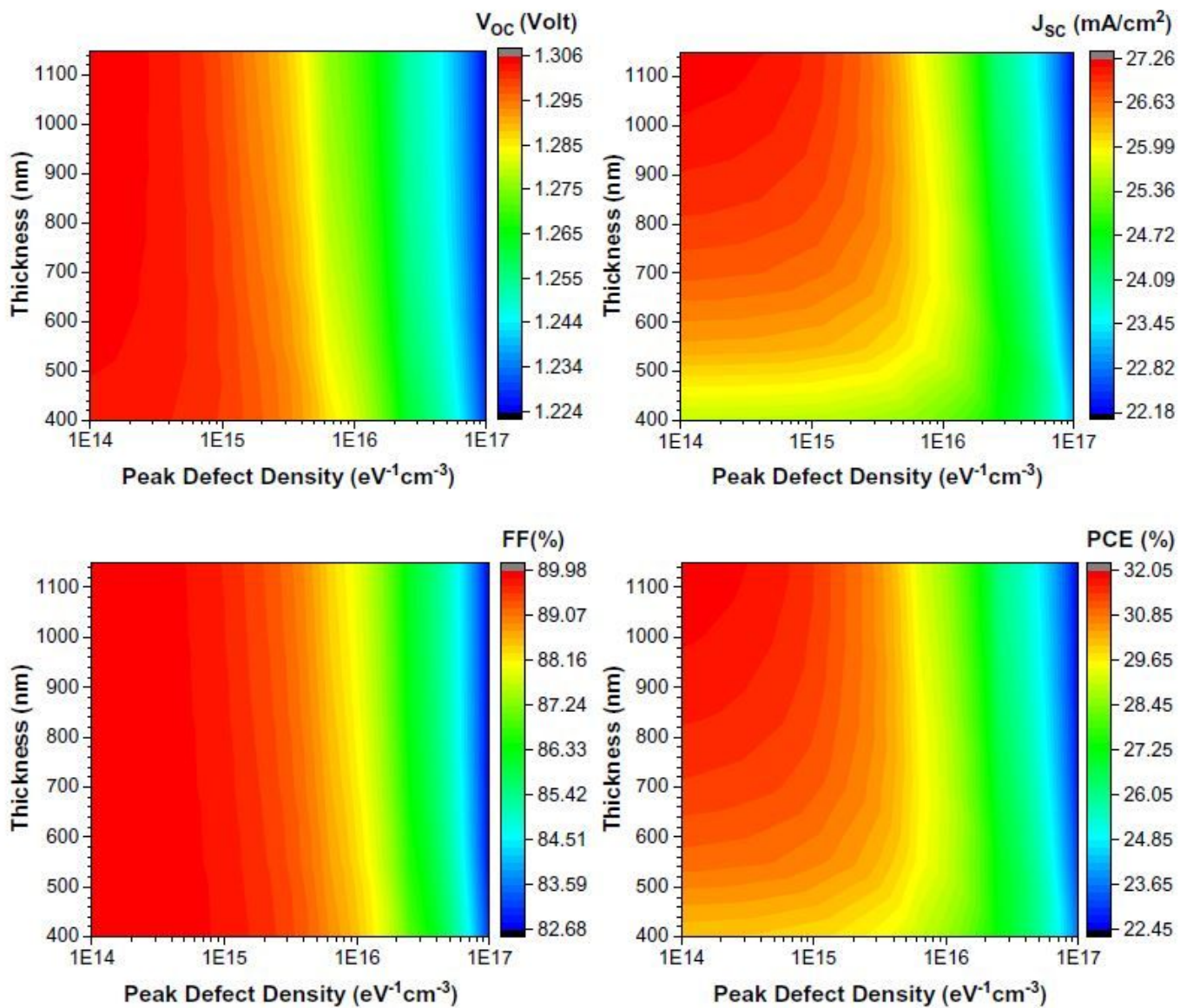


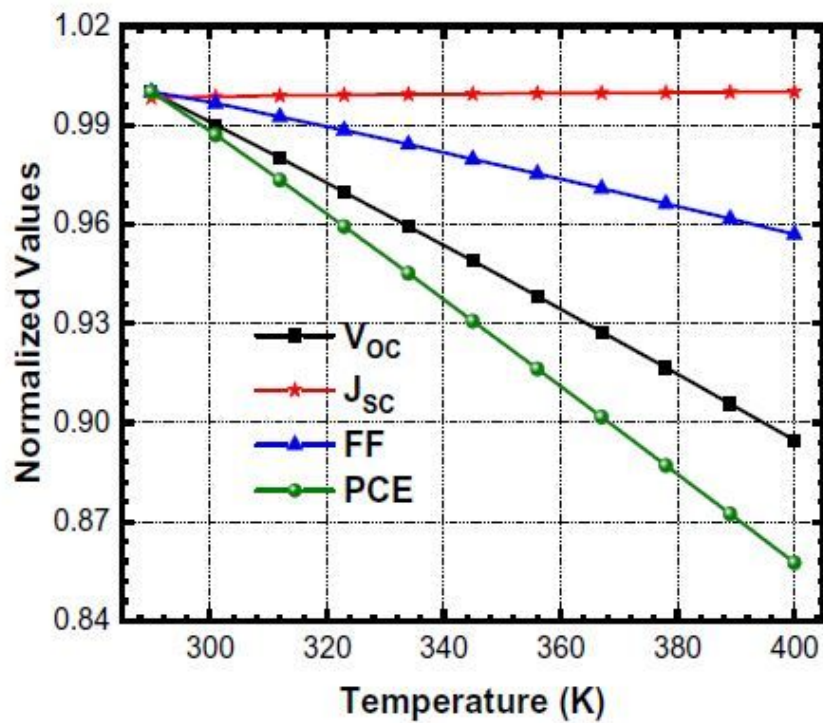
Figure 6

Normalized values of all PV performance parameters of the PSC as a function of acceptor concentration of the LHM layer.

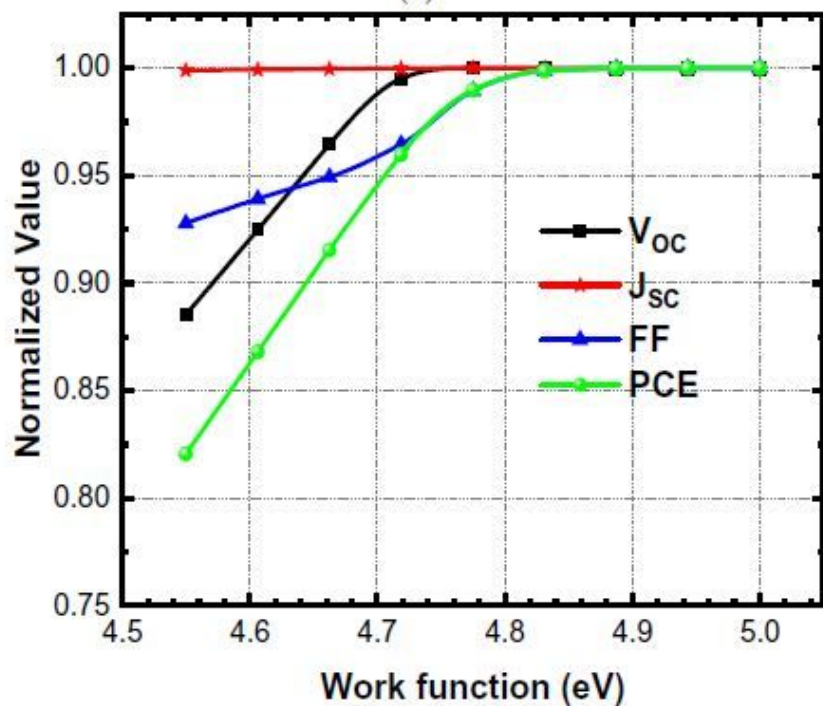


**Figure 7**

Contour graphs of PSC performance parameters dependency on of  $CH_3NH_3PbI_3$  LHM layer defect density and thickness.



(a)



(b)

Figure 8

Normalized values of all the PV performance parameters of the PSC as a function of (a) working temperature (b) back-contact metal work function.